Stability Analysis and Performance Improvement of Power Sharing Control in Islanded Microgrids

Li Sun, *Member, IEEE,* Xiaowei Zhao, Yongfeng Lv

***Abstract*—Due to the requirement of synchronism and power sharing, droop control and its variations have become one essential component for distributed generator (DG)-powered microgrids. However, the power sharing accuracy and system stability margin may be threatened by the randomness from the load demand and renewable generation. In this paper, a dynamic stability analysis is first performed on a DG-powered microgrid through a produced system frequency response model (SFR). The results point out that (i) the critical system eigenvalues directly vary with the system operating condition; (ii) a fixed-gain power sharing control is prone to be less damped and loses stability easily under some operating conditions. Then, the heuristic adaptive dynamic programming (HDP) strategy is used for power sharing control with the benefit of adapting to real-time disturbances and uncertainties. Through Lyapunov theorem, stability analysis is provided to demonstrate the reliability of the HDP-based power sharing control in islanded microgrids. Finally, simulation tests verify the analysis results and demonstrate the favorable performance of the HDP-based power sharing control under uncertain load disturbances.**

***Index Terms*—Distributed generator, dynamic stability, heuristic adaptive dynamic programming (HDP), islanded microgrid, power sharing.**

I. Introduction

Microgrids have been growing drastically as an alternative approach for coordinating distributed generators (DGs) and local loads to achieve grid-disconnected/islanded operation [1], [2]. DGs (such as photovoltaic (PV) plants and wind turbines) mostly work with power electronic interface and use phase-locked loop (PLL) for synchronization control [3], [4]. In islanded applications, parallel-connected DGs are often required to operate in an autonomous fashion and share the load proportionally [2]. This is done by the pre-curtailment control and power sharing control. The pre-curtailment control enables DGs to increase output when needed to provide "upward" reserves [4]. However, it is essential to make a compromise between technical considerations and economic factors when defining how much the power curtailment is (not detailed in this study). The power sharing control is commonly based on $P-f$ and $Q-V$ droop concept [5]–[7]. It is deployed in order of seconds and spontaneously offsets the system power imbalances. Over the years, there are devious droop control variations to broaden the spectrum of applicability [8].

This work was funded by the UK Engineering and Physical Sciences Research Council under grant EP/S001905/1.

L. Sun is with the School of Mechanical Engineering and Automation, Harbin Institute of Technology, Shenzhen 518055, China (email: sunli2021@hit.edu.cn)

X. Zhao (corresponding author) and Y. Lv are with the Intelligent Control & Smart Energy (ICSE) Research Group, University of Warwick, Coventry, CV4 7AL, U.K. (e-mail: xiaowei.zhao@warwick.ac.uk;Lyu@warwick.ac.uk).

It is much more relevant to cope with the limitations of $P-f$ and $Q-V$ droop methods during islanded applications, including the steady-state frequency and voltage deviation, power quality problems, and narrow stability margins [9], [10]. Some remedial solutions have been reported to cope with such limitations. In [11], additional derivative P and Q terms provide another freedom to enhance the $P-f$ and $Q-V$ droop stability, without affecting the power sharing performance. However, the derivative loops intensify the noises and impose impulses to the system. In [12], the hierarchical droop-based control has been developed to include the restoration mechanism of the system frequency and voltage deviations. Reference [13] upgrades this type of control scheme via a radial basis function neural network. However, the hierarchical control schemes are instinctly sluggish due to multiple control layers. Reference [14] proposes a novel droop control (named as PID power control) by replicating the autonomous frequency control for synchronous generators (SGs). The P-frequency/$\dot{V}$ term guarantees the proportional power sharing among DGs, the I-frequency/$\dot{V}$ term erases the frequency/voltage offset, and the D-frequency term contributes to better controllability and transient performance. While [14] points out that the PID power control effectiveness is related to the system operating condition, there is a lack of the impact mechanism analysis of the PID settings on the system stability by considering the system operating condition change.

As such, this paper attends to further investigate the dynamic analysis and improvement ways of $P-f$ and $Q-V$ droop power control in islanded microgrid applications. Small-signal stability analysis has been extensively applied in the field of microgrid control parameter determination [12], [15]–[18]. These reported papers mostly employ the eigenvalue-based analysis approach. A full-order or reduced-order (by neglecting the fast DG states) model is built with a matrix formation. Followed by the system matrix model, participation factor or other reasonable indexes can be defined to predict the impact of system parameters on the dynamic stability of the microgrid. However, the analysis results in [15]–[18] are lack of mechanism explanation on a specific control design accounting for the microgrid stability. Thus, it is still hard to understand the behaviors of DG-powered microgrids due to the control complexity. On the other hand, some efforts have been made to improve the control performance under large transient events. For example, [19] proposes to stabilize the microgrids following Lyapunov-based stability studies. However, the reported schemes in these papers acquiescently adopt fixed gains, in compliance with the stiff regulation requirement (to ensure a proportional power sharing). A notable drawback

is that the fixed-gain control is hard to conserve the microgrid stability in case of frequent and random operating condition changes (as explained in Section III. D).

In this context, research is limited to the dynamic stability issues of the PID power control proposed in [14] (Note, "dynamic stability" is introduced here to denote the small-disturbance stability in the presence of automatic controls [20]). The question is explored here to offer the industry and system operators a clearer understanding on stabilizing islanded DG-powered microgrids. As well known, system frequency response (SFR) modelling is commonly used for dynamic stability analysis and frequency control design of SGs in conventional power systems [20], [21]. The SFR model offers an intuitive way to illustrate the relation between system frequency behaviors and frequency control settings, and to describe their relation using a mathematical formulation. In view of this, our study first develops the SFR model of a DG-powered microgrid. It allows to provide a principal explanation on the relationship between PID power control settings and the dynamic system responses, by considering the operating condition change.

Furthermore, the heuristic adaptive dynamic programming (HDP) is introduced to improve the power control effectiveness during uncertain disturbances. HDP is built on the model-free framework with the neural network implementation. And it has been already reported in a number of industrial applications (like robotics, aircrafts, chemical processes, and smart grids [22]–[24]). It is hence foreseen to apply the HDP technology for the power sharing control problem in islanded microgrids.

This paper is organized as follows. Section II discusses the configuration and stability of $P-f$ and $Q-V$ droop based DGs in islanded applications. In Section III, a SFR model for a 2-DG test system is established. The proposed SFR model is then used to examine the relationship between the critical system eigenvalues and the power control settings as well as the operating conditions. Section IV describes the implementation of the proposed HDP based power control and conducts a stability analysis through Lyapunov theorem. Section V presents the simulation tests to verify the theoretical analysis and demonstrate the proposed control effectiveness. Finally, conclusions are drawn in Section VI.

II. Power Control for DGs in Islanded Microgrids

A. Control Architecture of DGs

A DG system may consist of different types of resources, such as biomass energy, wind turbines, and PV arrays. The physical and electrical parts of each DG are bridged by a dc link that decouples the dynamics of such two parts. Thus, the physical part is commonly cast as a power source and interfaces the external grid through an inverter. Fig. 1 illustrates a 2-DG islanded microgrid system, where the general configuration of DG control system is also included. It adopts a decoupled active and reactive power control. The power control is traditionally based on the $P-f$ and $Q-V$ droop concept. It enables DG to help preserve the frequency/voltage within tight tolerances and maintain a proportional load sharing between DGs. However, it is hard to maintain the frequency stability for a DG working in an islanded mode. This is explained as follows.

1) Islanded operation of $P-f$ and $Q-V$ droop based DGs: For ease of simplicity, we assume that $\boldsymbol{V_1}$ is stemmed from DG1 while $\boldsymbol{V_2}$ is absent in Fig. 1 (DG2 is not considered in this segment). Let the feeder line impedance $Z_1 = R_1 + j\omega L_1$ and the load impedance $Z_L = R_L + j\omega L_L$. The PCC voltage $\boldsymbol{V}$ is written as

$$V\angle\theta = \frac{Z_L}{Z_1+Z_L}V_1\angle\theta_1 = K_1V_1\angle(\theta_1 + p_1(\omega)) \quad (1)$$

where $K_1 = \left|\frac{Z_L}{Z_1+Z_L}\right|$ and $p_1(\omega) = phase(\frac{Z_L}{Z_1+Z_L})$. K_1 is the equivalent coefficient and $p_1(\omega)$ is the the phase-shift angle at the frequency ω. Using Park transformation, the input of the PLL PI compensator can be written as

$$V_q = K_1V_1\sin(\theta_1 + p_1(\omega) - \theta_p) = K_1V_1\sin(\Delta\theta_1) \quad (2)$$

where $\theta_1 = \eta + \theta_p$ and $\Delta\theta_1 = \eta + p_1(\omega)$ since the power angle η is controlled and estimated in PLL coordinate frame [25]. Following [25], the islanded DG system is stable if and only if

$$V_q = 0 \Rightarrow \Delta\theta_1 = \eta + \zeta + p_1(\omega) = 0 \quad (3)$$

can be automatically secured. Therein, ζ accounts for any additional time delay in producing the power angle.

Fig. 2 is used to present the PLL synchronization mechanism of an islanded DG. Two feedback loops contribute to generating the DG frequency. (i) Loop 1 is a 1^{st}-order positive feedback of ω through the load and PLL; (ii) Loop 2 may be a 1^{st}-order (when $P-f$ droop engages) or 2^{ed}-order (when PID power control engages) negative feedback of ω through the converter and PLL.

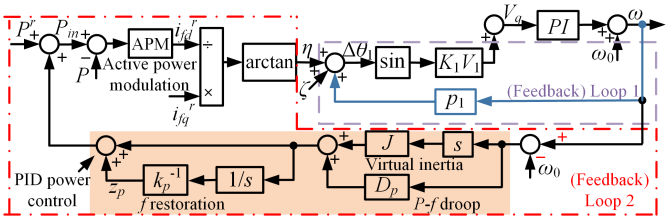

Figure 2. Frequency feedback of a DG through PLL and $P-f$ loop.

2) Stability estimation of $P-f$ and $Q-V$ droop based DGs: In islanded applications, the power angle η provides a freedom to fulfill (3). However, a negative η is hard to be timely produced once a $P-f$ droop based DG loses the utility frequency. This is due to a lack of supporting the transient response through the $P-f$ droop. A non-zero $\Delta\theta_1$ would be accordingly caused by ζ and the perturbation $p_1(\omega)$. The DG frequency ω keeps increasing or decreasing when $\Delta\theta_1$ is positive or negative. What's more, Loop 2 going through the power control has a time constant one or two orders larger than PLL. Thus, the DG frequency may be driven away by the fast-respond positive feedback loop (Loop 1) [26] and a frequency collapse may occur.

It is crucial to improve the transient performance of the $P-f$ and $Q-V$ droop-based power control. In this sense, the

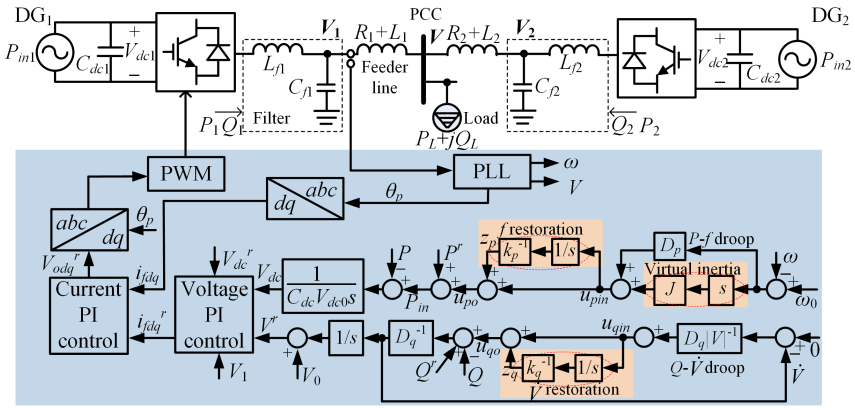

Figure 1. An islanded system with 2 DGs integrated.

PID power control [14] is introduced to maintain the operation stability of DGs in an islanded mode. As shown in Fig. 1, the introduced control consists of a $P-f/Q-\dot{V}$ droop (i.e., P-control), an $f/\dot{V}$ restoration loop (i.e., I-control) and a virtual inertia loop (i.e., D-control) [14]. The corresponding power control equations are given by Equation (5) in the next subsection. Compared to the conventional $P-f$ and $Q-V$ droop control, the PID frequency/voltage control also includes the $f/\dot{V}$ restoration and a virtual inertia loop that empower DGs to undertake the frequency/voltage offset elimination and the frequency/voltage transient performance improvement.

For DGs, the PID based power control should be designed with a relatively small bandwidth (around 2Hz), due to the requirements of high power quality injection and measuring filter design [11]. The followed DC-/AC- voltage control loop typically has a bandwidth around 20Hz that is at least five to ten times slower than that of the inner current control loop. Thus, the outer power control dictates the low-frequency dynamics of the inverter due to the timescale separation between the power and the voltage, current dynamics.

B. $P-f$ and $Q-\dot{V}$ Droop Control

The PID power control in Fig. 1 is inspired from the behavior of synchronous generators (SGs) in the bulk utility grid where the increasing output power leads to frequency (rotor speed) decline. Fig. 3 describes SGs' swing equation and frequency control block. The spin inertia (J_g, typically $4-20s$ [20]) makes the frequency decline slow down; the P-frequency control (with a gain K_p) helps lift the frequency nadir; and the I-frequency control (with a gain K_i) is in charge of the frequency restoration. G_{gov} represents the governor and turbine dynamics with a relatively large time constant, so that it can be cast as constant while studying the rotor dynamic. Thus, the transfer function of SGs' frequency regulation, from $\Delta\omega$ to ΔP, has a simplified expression as

$$\Delta\omega = -\frac{s}{J_g s^2 + K_p s + K_i}\Delta P \tag{4}$$

On the other hand, the $P-f$ and $Q-\dot{V}$ control for DGs

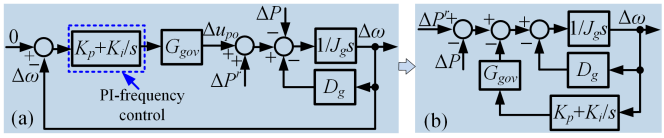

Figure 3. Control block of SGs' frequency regulation.

(see Fig. 1) has a conceived control law [14]

$$J\dot{\omega} + D_p\omega = -u_{po} \tag{5a}$$
$$k_p\dot{z}_p = J\dot{\omega} + D_p\omega \tag{5b}$$
$$D_q|V|^{-1}\dot{V} = -u_{qo} \tag{5c}$$
$$k_q\dot{z}_q = D_q|V|^{-1}\dot{V} \tag{5d}$$

Mostly, the power supply from the power source should provide the needed energy of the inverter as fast as possible. This implies that $P_{in} = P$ and $Q_{in} = Q$. Thus, (5) has an equivalent form in the concept of small-signal modelling, expressed as

$$J\Delta\dot{\omega} + D'_p\Delta\omega + k_p^{-1}D_p\int\Delta\omega = \Delta P^r - \Delta P \tag{6a}$$
$$D_q|V|^{-1}\Delta\dot{V} + k_q^{-1}D_q|V|^{-1}\int\Delta\dot{V} = \Delta Q^r - \Delta Q \tag{6b}$$

where $D'_p = D_p + k_p^{-1}J$. The superscript r denotes the reference value of variables. It is apparent that $P-f$ (see (6a)) and $Q-\dot{V}$ (see (6b)) control are indeed a PID and PI control, respectively. That is, the $P-f$ and $Q-\dot{V}$ control parameters could be optimized following the PID control optimization method. In this paper, authors have been dedicated on a compromise between the accurate power sharing and better damping power mode fluctuations, and accordingly discussion will be limited to active power loop only. In addition, PI control is a special case of PID control, thus the optimal design of $Q-\dot{V}$ could be referred to the $P-f$ control optimization process. For conciseness, the voltage stability is then cast to be preserved during an operating interval through using local reactive power compensators.

III. SFR Model and Design Requirements of PID Power Control Based DGs

As mentioned in Section II, PID power control based DGs provide the freedoms to maintain proportional power sharing, improve transient response and avoid any frequency deviation. This section demonstrates the dynamic stability of PID power control based DGs dependent on the PID control settings, line impedances and operating conditions. It is based on an examination of the dynamic frequency behaviors using the system frequency response (SFR) model. The requirements on PID control settings are established and further confirmed by small-signal stability studies.

A. 2-DG Test System

For ease of theoretical analysis, we consider a 2-DG connected local load system in Fig. 1. Reference [9] has pointed out that (i) a grid-forming DG with the multi-loop droop control (constituted by a cascaded outer power control and inner voltage & current control) properly bolsters the inverter filter capacitor voltage $\boldsymbol{V_1}/\boldsymbol{V_2}$ and makes it approximately a controllable voltage source; (ii) the fast inner voltage & current control compensates for the function of the filter inductance (L_{f1}/L_{f2}) as a coupling reactance, so its variation does not have an impact on the output impedance. On this basis, (i) (6a) is able to describe the motion of the voltage angle θ_1/θ_2; (ii) the line impedance has a dominant role in preserving the test system stability, while the impact of the filter inductance is hidden by the inner voltage & current control.

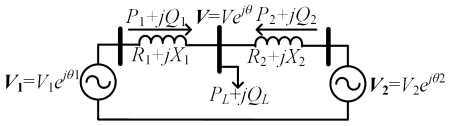

Figure 4. Equivalent circuit model of the 2-DG test system.

B. Frequency Response Model

The test system has an equivalent circuit model as shown in Fig. 4. R_1, X_1 and R_2, X_2 represent the line resistance and reactance of DG1 and DG2, respectively. The power equations of DG1 and DG2 can be written as

$$P_i = \frac{R_i}{Z_i}\left[\frac{V_i V}{Z_i}\cos(\theta_i-\theta)-\frac{V^2}{Z_i}\right]+\frac{X_i}{Z_i}\frac{V_i V}{Z_i}\sin(\theta_i-\theta) \quad (7)$$

where $i = 1$ or 2 represents the two branches in the simplified circuit; $Z_i = \sqrt{R_i^2+X_i^2}$ is the magnitude of the line impedance. Perturbing (4) yields

$$\Delta P_i = K_i(\Delta\theta_i - \Delta\theta) \quad (8)$$

$$K_i = \frac{V_{i0}V_0}{Z_i^2}\left[-R_i\sin(\theta_{i0}-\theta_0)+X_i\cos(\theta_{i0}-\theta_0)\right] \quad (9)$$

In addition,

$$\Delta P_1 + \Delta P_2 = \Delta P_L \quad (10)$$

where ΔP_L is the given load perturbation. Using (6) and (7)-(10), the SFR model is established as shown in Fig. 5. It is able to represent the dynamic behaviors of the test system. Note that the control design (see Fig. 1 and (6)) of DGs is modified such that it resembles the input-out characteristic of SGs (see Fig. 3(b)) while still preserving the original dynamical properties. The scalability of SFR modeling for a multiple-DG system is discussed in Appendix. A. Following [20], [27], using the SFR model of 2-DG system is enough to reveal the impact mechanism of the frequency control on the system dynamic stability. In this sense, the 2-DG SFR model would be hence used for the followed theoretical analysis, instead of the multiple-DG SFR model with much more complexity.

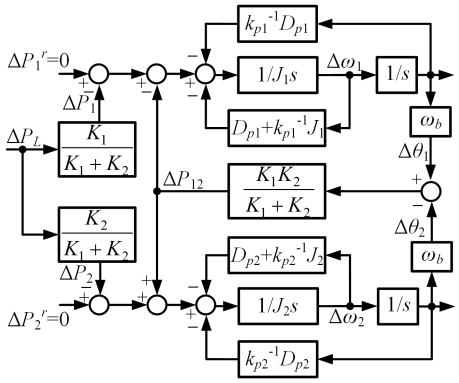

Figure 5. SFR model of the 2-DG test system.

C. Stability Analysis and Design Requirements

From Fig. 5, the dynamic of the frequency ω_1 under the load perturbation ΔP_L can be described by

$$\Delta\omega_1 = \frac{-sK_1(G_2(s)+K_2)\Delta P_L}{K_1G_1(s)(G_2(s)+K_2)+K_2G_2(s)(G_1(s)+K_1)} \quad (11)$$

where $G_i(s) = J_is^2+(D_{pi}+k_{pi}^{-1}J_i)s+k_{pi}^{-1}D_{pi}$ ($i = 1$ or 2) represents the PID frequency control action. According to [14], the control parameters (D_{pi}, k_{pi} and J_i) based on the DG_i's rating should be the same to maintain the power sharing accuracy between DGs. For convenience, the notations D_p, k_p and J are used to denote the PID power control parameters for all DGs in what follows. It means that $G_1(s) = G_2(s) = Js^2+(D_p+k_p^{-1}J)s+k_p^{-1}D_p = G(s)$. Thus, (11) becomes

$$\Delta\omega_1 = -\frac{sK_1(G(s)+K_2)}{(K_1+K_2)G(s)(G(s)+2K_{12})}\Delta P_L \quad (12)$$

where $K_{12} = \omega_b\frac{K_1K_2}{K_1+K_2}$. Manipulating (9) gives that

$$\Delta\omega_1 = -\frac{1}{2}\left[\frac{K_1-K_2}{K_1+K_2}\frac{1}{G(s)+2K_{12}}+\frac{1}{G(s)}\right]s\Delta P_L \quad (13)$$

Consider $G(s) = J_s^2+(D_p+k_p^{-1}J)s+k_p^{-1}D_p$, some important findings can be obtained

- The moment of inertia J_g (in (4)) helps the rotor mass release/absorb the kinetic energy and provides fast response to disturbances. This phenomenon gives time for the frequency control to respond and rebalance the power supply and demand. By contrast, the presence of D-frequency control in DGs could be regarded as a virtual inertia J (in (13)), which can be assigned at a desired value differing from the physical rotor inertia.

- The P-frequency control (with an equivalent gain $D_p + k_p^{-1}J$) arrests the frequency decline and partially restores frequency to enter tight tolerances. In conventional power systems, the P-frequency control ensures the power sharing between SGs, suppresses oscillations, and helps SGs to be in synchronism with the power grid. This underlying mechanism has been immigrated for parallel-connected DGs in an islanded microgrid.
- The I-frequency control (with an equivalent gain $k_p^{-1}D_p$) is used to completely restore frequency and return the grid to normal operation. To ensure the control system to be effective and stable, the I-frequency control gain is usually assigned at a small value.

The following criteria should be considered when selecting the appropriate PID settings for DGs:

- The I-frequency control upgrades the frequency restoration capacity with an assigned gain $k_p^{-1}D_p$. k_p^{-1} and D_p both have a maximum allowable value to ensure the effective gain not too large.
- The updated droop gain is given as $(D_p + k_p^{-1}J)$. So, D_p should not be too small to comply with the requirements of power sharing response and damping effect. In addition, the accurate power sharing still needs to be established and leads to

$$\frac{P_1}{D'_{p1}} = \cdots = \frac{P_i}{D'_{pi}} = \cdots = \frac{P_n}{D'_{pn}} \tag{14}$$

  where $D'_p = D_p + k_p^{-1}J$.
- The inertia gain J provides a freedom to resist changes in frequency and to improve the dynamic response. Consider a step load increment (with a magnitude of P_d). Revisiting (13), $\Delta\omega_1$ evolves with the time

$$\begin{aligned}\Delta\omega_1(t) = &-\frac{1}{2}\frac{K_1 - K_2}{K_1 + K_2}\frac{P_d}{J\omega_d}e^{-\frac{D'_p}{2J}t}\sin\omega_d t \\ &-\frac{1}{2}\frac{P_d}{D_p - k_p^{-1}J}(e^{-k_p^{-1}t} - e^{-D_p J^{-1}t})\end{aligned} \tag{15}$$

  associated with $\omega_d = \omega_n\sqrt{1-\xi^2}$, $\omega_n^2 = J^{-1}(k_p^{-1}D_p + 2K_{12})$ and $2\xi\omega_n = D_p J^{-1} + k_p^{-1}$.

(15) reveals that (i) the steady-state frequency deviation is in around proportional to the power disturbance with a coefficient of D_p^{-1} under the assumption that $D_p \gg k_p^{-1}J$ (Note that D_p has no impact on the dynamic frequency response when $J = 0$); and (ii) the inertia J allows us to shape the transient frequency response while keeping the static droop characteristics. Therefore, the droop gain D_p fixes the steady-state droop function (subject to the requirement in (14)), whilst J and k_p are selected to guarantee good transient response and stable frequency restoration.

In what follows, a small-signal analysis is conducted to provide a better understanding of the role of the power control parameters in determining the system stability. A full-order model of the test system is established in Matlab/Simulink. The Model Linearizer is adopted to clearly illustrate the critical eigenvalue immigration along with the control parameter settings. DG1 and DG2 are identical and rated at 2MW and 575V. In all cases, we let $L_{f1} = L_{f2} = 0.2$pu, $C_{f1} = C_{f2} = 0.057$pu, the PID-frequency control parameters (D_p, k_p, J) initially at (15, 1, 2), the time constant (T_d) of the washout filter (that is used to emulate the derivative term in D-control) at 0.1. The line has a low X/R ratio at 3.427 ($X_l = 0.3951\Omega/km$, $R_l = 0.1153\Omega/km$ [28]). Other key parameters associated with DGs are referred to [28].

Table I
CRITICAL EIGENVALUES AND PARTICIPATION FACTOR (PF) CALCULATING

Critical eigenvalues of the 2-DG test system

$\lambda_{1,2}$	$\lambda_{3,4}$	$\lambda_{5,6}$	$\lambda_{7,8}$	$\lambda_{9,10}$
$-17.8 \pm j307$	$-15.8 \pm j64$	$-12.4 \pm j22.9$	$-10.3 \pm j7.98$	$-1.12 \pm j2.84$

For the two DGs, $P_{10} = P_{20} = 0.958$pu. The critical eigenvalues that significantly affect stability are tabulated in Table I. The real eigenvalues and the other eigenvalues that are far away from the imaginary axis are not presented in this context. Fig. 6 depicts the immigration of the critical eigenvalues with the control parameters. It shows that

- D_p should not be relatively small subject to the low-frequency stability of $\lambda_{9,10}$, and meanwhile it has a maximum allowable value accounting for the PLL and power control stability of $\lambda_{3,4}$. Thus, D_p is selected by considering a compromise between the fast response and stability requirement.
- Increasing k_p^{-1} drives both $\lambda_{3,4}$ and $\lambda_{7,8}$ to the right. This means that k_p^{-1} should not be set at a relatively large value.
- The inertia control has two concerned parameters that significantly impact the system stability. For a small time constant T_d ($= 0.1$), the range of the gain J is limited since increasing J easily provokes the DC-link mode $\lambda_{1,2}$ to the right half s-plane (RHP) of the root loci spectrum while a smaller J causes the power control mode $\lambda_{7,8}$ toward the RHP. By increasing T_d to 1, a large inertia J and stability margin can be ensured. However, a large T_d leads to a delayed inertial response for DGs. Thus, it is crucial to make a trade off between the stability margin and the inertia requirement when selecting the inertia control parameters.

D. Consideration of the Impact of the Operating Condition

The presence of coefficients K_1, K_2 in (15) admits that the frequency dynamic will be significantly impacted by the operating condition. That is, the system frequency stability may be hard to be preserved for a conventional PID frequency control, although it is well-designed compliance with the stiff regulation requirement at a specific operating condition. This is examined in details hereafter.

Revisiting (12), its eigenvalue equation is obtained as

$$G(s)\left[Js^2 + (D_p + k_p^{-1})s + k_p^{-1}D_p + 2K_{12}\right] = 0 \tag{16}$$

(16) generates four eigenvalues. The former two eigenvalues originated from $G(s)$ are just determined by the PID control parameters, while the latter two eigenvalues created by

$$Js^2 + (D_p + k_p^{-1})s + \underbrace{k_p^{-1}D_p + 2K_{12}}_{\text{constant term}} = 0 \tag{17}$$

By calculating (17), the concerned critical eigenvalues are

$$\lambda_{c1,c2} = -\xi\omega_n \pm j\sqrt{1-\xi^2}\omega_n \tag{18}$$

that would directly vary with the operating condition (through the coefficient $K_{12}(= \omega_b K_1 K_2/(K_1 + K_2))$, even if the regulation requirements are applied to select the PID control parameters. The properties of the critical eigenvalues (18) are examined by considering the following three cases.

- The ratio X_i/R_i is very high and the impact of R_i can be omitted. In this case, K_1 and K_2 are both positive, making the constant term in (17) stay positive. The concerned eigenvalues (18) could be kept in the left half s-plane (LHP). It is of interest to note that a relatively large K_1 and K_2 (thus K_{12}) are obtained for a small X_i, creating the condition where the test system is prone to be less damped (ω_n increases but ξ decreases from (15)) and loses stability more easily under some circumstances. This is the same to the result drawn in [9] and needless to repeat in this context.
- The ratio X_i/R_i is not very high, usually appearing for a low-voltage microgrid distribution line [28], [29]. If the power angle ($\theta_{i0} - \theta_0$, $i = 1$ or 2) is small enough, K_1 and K_2 could be still kept positive. The concerned eigenvalues (presented by (18)) hence always stay in the LHP. However, the test system has a threat of losing stability under the case of a relatively small R_i and X_i.
- For a low X_i/R_i and a large power angle ($\theta_{i0} - \theta_0$), K_1 and K_2 would become negative (refer to (6)). This creates a condition where the constant term in (17) becomes negative if $k_p^{-1}D_p < -K_{12}$. One of the concerned eigenvalues hence shifts to the RHP, posing a threat to frequency stability. This effect is worse under a heavily loading condition and a loosely-interconnected network.

Revisiting the small-signal analysis on the full-order model of the 2-DG test system, Fig. 7 illustrates the immigration of the critical eigenvalues along with DGs' operating condition.

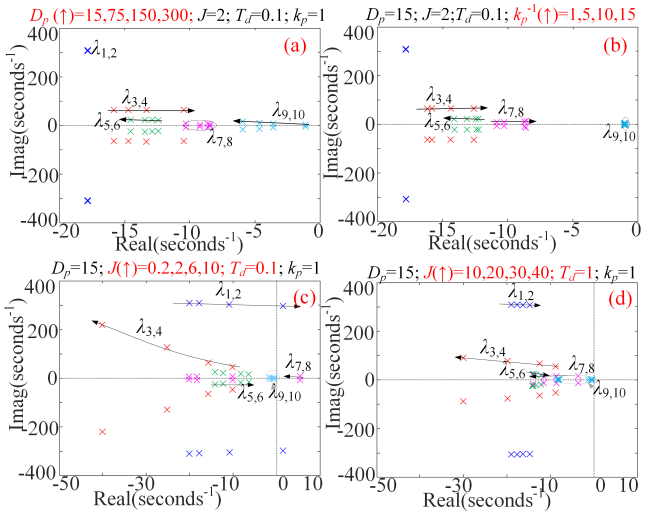

Figure 6. Critical eigenvalues of the test system varying with the PID power control parameters (the arrow of the respective critical eigenvalues indicating the direction of their movement).

(i) Under a lightly loading condition, the eigenvalues $\lambda_{1,2}$ and $\lambda_{3,4}$ both move left along with increasing the power angle; $\lambda_{5,6}$ move right but their stability is maintained in this process. (ii) Under a heavily loading condition, $\lambda_{1,2}$ move left when increasing the power angle, but $\lambda_{3,4}$ move right and even enter the RHP; the remainder eigenvalues are less susceptible to the change of the operating condition. Thus, the test system has a threat of losing stability when a large power angle is created under a heavy load condition and a long interconnecting line.

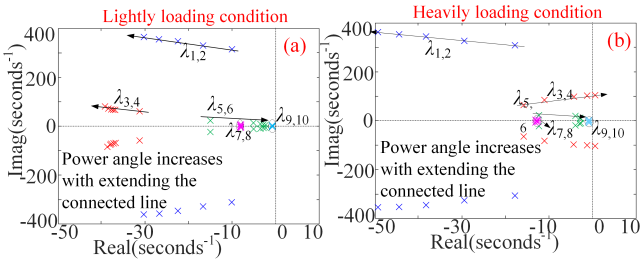

Figure 7. Critical system eigenvalues under different operating conditions ($X_i(\uparrow) = 10X_l, 20X_l, 30X_l, 40X_l, 50X_l$): (a) $P_{10} = P_{20} = 0.479$ pu and (b) $P_{10} = P_{20} = 0.958$ pu.

Remark 1:

- The immigration of the critical eigenvalues significantly depends on the operating condition; this is at the expense of the stability margin of these eigenvalues. The fixed-gain PID power control, in light of the stiff regulation requirement, is typically designed to ensure a proportional power sharing and good frequency performance at one operating condition.
- The PID parameters can be designed offline by possible disturbances through intelligent algorithms (such as particle swarm optimization (PSO) or genetic algorithm (GA)). With the target frequency stability and power constraints, the PID control parameters can be set to guarantee the stability of the critical eigenvalues along a wide range of loading trajectory.

Remark 2:

- When uncertain disturbances appear, the fixed-gain PID power control struggles to effectively preserve the system frequency quality and the power sharing among DGs.
- The adaptive control method is very necessary and significant to online cope with the real-time and uncertain load disturbances in islanded microgrids.

IV. HDP-PID Power Control for DGs in Islanded Microgrids

In this section, a HDP-PID power control scheme is developed to improve the power sharing performance and system stability under frequent and uncertain disturbances. Using a Lyapnov approach, it shows that the developed adaptive power sharing control retains the property of uniformly ultimate boundedness (UUB) (with the definition referred to [30]) under mild conditions.

A. Feedforward Neural Network of HDP

In what follows, a HDP-PID power control is developed to enable DGs the inertia support and power buffer in an online learning way. Fig. 8 displays a generalized version of the neural network for HDP, with one hidden layer. Notably, the input states x_i $(i = 1, \ldots, m)$ are augmented at the hidden layer, so that the network outputs y_k $(k = 1, \ldots, n)$ are function of the augmented states. m and n are the neuron number of the inputs and outputs, respectively. Let p_k, and q_k denote the input and output of a hidden node, respectively. In addition, $\phi(\cdot)$ denotes a hyperbola tangent threshold function.

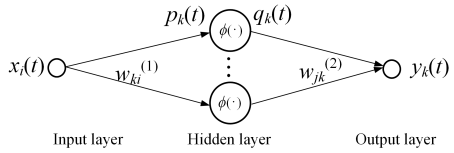

Figure 8. Feedforward neural network.

Refer to Fig. 8, we have

$$p_k = \sum_{i=1}^{m} W_{ki}^{(1)} x_i,\ q_k = \phi(s_k),\ y_k = \sum_{i=1}^{N_h} W_{jk}^{(2)} q_k \tag{19}$$

The relationship of y_k and x_k can be produced by (19). In a compact form, we get

$$y = W^{(2)T} \phi(W^{(1)} x) \tag{20}$$

It was discovered in [31] that the input-to-hidden layer weights $W^{(1)}$ are chosen initially at random and kept constant and if N_h is sufficiently large, then the neural network approximation error can be made arbitrarily small since the activation function vector forms a basis. Therefore, only the output weights $W^{(2)}$ are proposed to be updated during learning. For ease of discussion, the subscripts "c" and "a" are introduced to indicate the variables for the critic and action network, respectively; the hidden-to-output weights for critic network and action network are denoted as W_c and W_a, respectively; the hidden layer neuron activation function vector y is denoted as $\phi(x)$ in what follows.

B. HDP-based Power Control Design

Define the Hamiltonian function as

$$H(x, u) = \dot{Y}(x) + r(x, u) \tag{21}$$

Therein, the performance index $Y(x)$ is defined as

$$Y(x) = \int_t^{\infty} r(x(\tau), u(\tau)) d\tau \tag{22}$$

It achieves its optimal value until $Y^*(x) = \min_u Y(x)$. The utility function $r(x, u)$ is expressed as

$$r(x, u) = x^T B x + u^T R u \tag{23}$$

where B and R are symmetric positive definite matrices with appropriate dimensions. The critic network learns from a reinforcement signal $r(x, u)$ to approximate the minimal cost function $Y(x)$. The action network produces the control action u by minimizing the approximated cost function $\hat{Y}(x)$. In what follows, the action and critic networks are both implemented using the neural network in Fig. 8. They perform the feed-forward calculation and the back propagation during the learning process. The proposed HDP-PID power control is shown in Fig. 9.

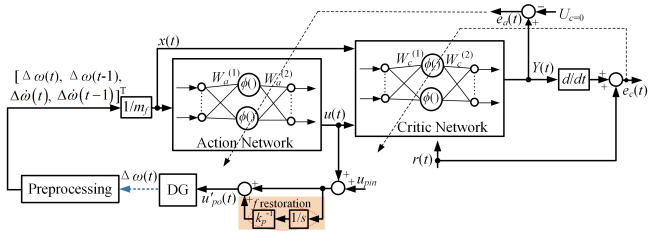

Figure 9. Schematic diagram of HDP-PID power control.

1) Critic network learning: The critical network attends to approximate $Y(x)$ as follows:

$$Y(x) = W_c^T \phi_c(x) + \varepsilon_c \tag{24}$$

where ε_c is the approximation error of critic network. The derivative of $Y(x)$ with respect to x is

$$\nabla Y = \nabla \phi_c^T W_c + \nabla \varepsilon_c \tag{25}$$

where $\nabla \phi_c \triangleq (\partial \phi_c(x)/\partial x)$ and $\nabla \varepsilon_c \triangleq (\partial \varepsilon_c / \partial x)$.

Let $\hat{W}_c$ be an estimate of W_c, it leads to $Y(x)$ having an estimate as

$$\hat{Y}(x) = \hat{W}_c^T \phi_c(x) \tag{26}$$

The critic network error e_c is derived as

$$\begin{aligned} E_c &= e_c^T e_c / 2 \\ e_c &= H(x, u, \hat{W}_c) = \dot{\hat{Y}}(x) + r(x, u) \end{aligned} \tag{27}$$

The weight for the critic network update in light of a gradient descent rule, which is given by

$$\dot{\hat{W}}_c = -l_c \sigma_c (\sigma_c^T \hat{W}_c + r(x, u)) \tag{28}$$

where $l_c > 0$ is the learning rate of critic network; $\sigma_c = \sigma/(\sigma^T\sigma+1)$, $\sigma = \dot{\phi}_c(x)$. There exists $\|\sigma_c\| \leq \sigma_{cM}$ (for a σ_{cM} larger than 1). For a fixed control policy u, the Hamiltonian function (24) becomes

$$H(x, u, W_c) = \dot{Y}(x) + r(x, u) = \varepsilon_h \tag{29}$$

Define the weight estimation error $\widetilde{W}_c = \hat{W}_c - W_c$. By using (25)-(27) and (29), (28) can be written as

$$\dot{\widetilde{W}}_c = -l_c \sigma_c (\sigma_c^T \widetilde{W}_c + \varepsilon_h) \tag{30}$$

2) Action network learning: The action network is trained to develop the feedback control policy. It approximates the control u as

$$u = \phi(v) + \varepsilon_a, v = W_a^T \phi_a(x) \tag{31}$$

where ε_a is the approximation error of action network. Let $\hat{W}_a$ be an estimate of W_a, the following can be yielded

$$\hat{v} = \hat{W}_a^T \phi_a(x) \tag{32}$$

The action network error e_a is defined is

$$E_a = e_a^T e_a/2, e_a = \phi(\hat{v}) + (1/2)R^{-1}B_u\nabla\hat{Y} \quad (33)$$

where B_u characterizes the relationship between x and u in the system state-space model. The weight update rule in the action network is a gradient descent algorithm, as shown by

$$\dot{\hat{W}}_a = -l_a\phi_a[\hat{W}_a^T\phi_a + (1/2)R^{-1}B_u\nabla\phi_c^T\hat{W}_c]^T \quad (34)$$

where $l_a > 0$ is the learning rate of action network. Define the weight estimation error $\widetilde{W}_a = \hat{W}_a - W_a$. Since the control policy in (31) minimizes the performance function $Y(x)$ in the infinite horizon, we have

$$\varepsilon_a + W_a^T\phi_a + (1/2)R^{-1}B_u(\nabla\phi_c^T W_c + \nabla\varepsilon_c) = 0 \quad (35)$$

by assumption that $\phi(v) = v$ for a relatively small v (referred to Theorem 1). Combining (34) and (35) yields

$$\dot{\widetilde{W}}_a = -l_a\phi_a[\widetilde{W}_a^T\phi_a + (1/2)R^{-1}B_u\nabla\phi_c^T\widetilde{W}_c + \varepsilon_{ca}] \quad (36)$$

where $\varepsilon_{ca} = -[\varepsilon_a + (1/2)R^{-1}B_u\nabla\varepsilon_c]$.

C. Stability Analysis

Before moving on, the following assumption is made, which can reasonably be satisfied under the current problem settings.

Assumption 1:

- The following notations involved in the HDP algorithm are upper bounded. That is, (i) $\|W_c\| \leq W_{cM}$, $\|W_a\| \leq W_{aM}$; (ii) $\|\varepsilon_c\| \leq \varepsilon_{cM}$, $\|\varepsilon_a\| \leq \varepsilon_{aM}$; (iii) $\|\phi_c(\cdot)\| \leq \phi_{cM}$, $\|\phi_a(\cdot)\| \leq \phi_{aM}$; (iv) $\|\nabla\varepsilon_c\| \leq \varepsilon_{dM}$, $\|\nabla\phi_a\| \leq \phi_{dM}$ and $\|\varepsilon_h\| \leq \varepsilon_{hM}$.
- The persistent excitation conditions for tuning critic and action network require that $\|\sigma_c\| \geq \sigma_{cm}$ and $\|\phi_a\| \geq \phi_{am}$ (σ_{cm} and ϕ_{am} are positive constants) [33].

Theorem 1: Let Assumption 1 hold and design the reinforcement signal as given in (23). Let the critic network output be given as (26) , and critic network weights update according to (28), action network weights update according to (34). Let the initial action network weights be chosen to generate an initial admissible control. And provided that the learning rate l_c and l_a fulfill the inequalities of (44). Then the weight estimate errors $\widetilde{W}_c$ and $\widetilde{W}_a$ are UUB. Furthermore, the obtained control input $\hat{u}$ is close to the optimal control input u within a small bound ε_u, i.e., $\|\hat{u} - u\| \leq \varepsilon_u$ as $t \longrightarrow \infty$ (herein, ε_u is a small positive constant).
The proof is referred to Appendix.

Remark 3: The principle of tuning the action network is to indirectly backpropagate the error between the desired ultimate objective (U_c) and the approximate performance function $\hat{Y}$ from the critic network. Thus, the feedback error signal e_a could be defined as

$$E_a = e_a^T e_a/2, e_a = \hat{Y} - U_c \quad (37)$$

where U_c is set as "0" without loss of generality [32]. While (37) is equivalent to (33), it allows to update the weight free of the system model. From [32], we have

$$\dot{\hat{W}}_a = l_a\left(-\partial E_a/\partial\hat{W}_a\right) \quad (38)$$

In what follows, (37)-(38) would be used as a substitute for (33)-(34) when obtaining the weight estimate $\hat{W}_a$.

Remark 4: The HDP-PID control stability is able to be preserved from the following two aspects:

- The proposed control through HDP networks offers a supplementary power correction signal. When disturbances and uncertainties happen, the $P-f$ droop control outputs the main control signal and the HDP network outputs the auxiliary control signal (see Fig. 9). Until the frequency deviation reaches zero, both control values become zero.
- The stability of the HDP-PID control mainly relies on the basic $P-f$ droop control. The HDP network usually sets the output limit, which is small and not enough to cause any instability. Additionally, the HDP algorithm has the uniformly ultimately bounded stability (see Theorem 1).

That is, the original fixed-gain PID control is mainly responsible for the stability and the HDP networks could greatly improve the control performance during uncertain disturbances.

V. Simulation Tests

A. Case Studies for Theoretical Analysis

In this subsection, we use the time-domain model of the 2-DG test system to demonstrate the analysis results presented in Section III. Each DG is an aggregated 2-MW full-converter wind turbine (refer to [28]). The rated power of each DG is 100 MW (50×2 MW). The mechanical system is represented by a power source, while the dynamics of power control, voltage & current control, PLL control, DC link, filter and interconnecting lines are all captured. The block diagram of a DG with a PID power control is shown in Fig. 1, with the PID control parameters initially set as $D_p = 15$, $J = 20$ and $k_p = 1$ (other key parameters of the DG system are referred to [28]). The interconnecting lines have a uniform X/R ratio at 3.427 ($X_l = 0.3951\Omega/km,\ R_l = 0.1153\Omega/km$) [28].

At all cases, $P_{10} = P_{20} = 0.958$pu, $X = 10X_l$; a load step change occurs in the test system at $t = 1s$. Fig. 10 shows the responses of DGs varying with the PID power control parameters. (i) The increase of D_p results in a higher oscillating frequency and a lifted frequency nadir. This is the consequence of a degraded PLL dynamic but an improved low-frequency dynamic. (ii) The increase of J drastically improves the dynamic frequency performance (leading to a smaller slope and a higher nadir during the frequency dropping). However, an undue value of J (such as $J = 300$) indeed provokes the frequency instability. (iii) For a larger k_p^{-1}, the frequency can quickly regain its normal value but may concomitantly manifest an aggravated oscillation. This is because that the increase of k_p^{-1} tends to deprave the damping of the PLL and PID control dynamics (see Fig. 6).

In Fig. 11, the responses of DGs varying with the operating conditions are presented (versus a load step change at $t = 1s$ in the test system). (i) When picking up a given heavy local load, a large power angle of DGs is created for a long interconnecting line. This accordingly causes a damage to the islanded microgrid stability. (ii) However, a smaller power angle of DGs is counted during lightly loading. DGs are more easily to conserve stability in this case.

Thus, results in Fig. 10 and Fig. 11 reveal that the small-signal analysis in Section III is able to predict the islanded microgrid stability and provides a guidance to circumvent the stability problems through tuning PID parameters. Some algorithms (like PSO or GA) can be then used to train the PID parameters offline with the frequency stability objective and power constraints. However, the fixed-gain PID power control is weak in addressing the real-time and uncertain load disturbances. To cope with this problem, an online HDP-based power control is developed. The control performance tends to be demonstrated in the next subsection.

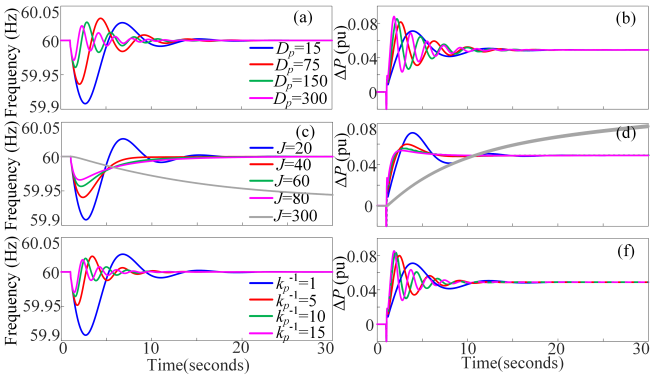

Figure 10. Responses of DGs varying with the PID settings. (Note: the output power ($\Delta P_1/\Delta P_2$) of DG1/DG2 is denoted by the solid/dashed line.)

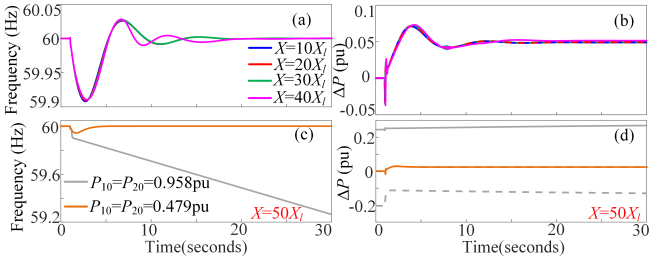

Figure 11. Responses of DGs varying with the operating conditions: (a)-(b) for a highly loading condition ($P_{10} = P_{20} = 0.958$pu); (c)-(d) for long interconnected lines ($X = 50X_l$).

B. Case Studies for HDP-PID Power Control

The input data consists of the current frequency deviation $\Delta\omega(t)$, the time-step delay variable $\Delta\omega(t-1)$, as well as their derivatives $\Delta\dot{\omega}(t)$ and $\Delta\dot{\omega}(t-1)$. These data are first normalized in [-1, 1] before proceeding HDP's neural network.

$$x(t) = \frac{1}{m_f}\left[\Delta\omega(t), \Delta\omega(t-1), \Delta\dot{\omega}(t), \Delta\dot{\omega}(t-1)\right]^T \quad (39)$$

where m_f is the normalization coefficient, determined by the maximal possible absolute value of the frequency deviation. The matrices B and R when generating the reinforcement signal $r(t)$ are set as $B = diag\,(1, 0.5, 0.05, 0.01)$ and $R = 1$. Once load disturbances or network topology changes appear, $r(t)$ grows with the increase of frequency deviation. This consequently updates the weights of both neural networks, thus the HDP-PID output signal u_{po} updates and adaptively reduce the impact of load and network topology changes.

The 2-DG and a modified IEEE 14-bus test system (see Fig. 12) are both used for the following case studies. DGs have the same control configuration and parameters in these two test systems (importantly, $D_p = 15$, $J = 20$, $k_p = 1$). Notably, the foremost is to demonstrate the control performance a severe operating condition where the test system operates with a heavy load and a loosely-interconnected network. Responses of DGs fitted with a conventional PID and the proposed HDP-PID power control are both displayed to reveal some insights into the necessity of an optimal control design.

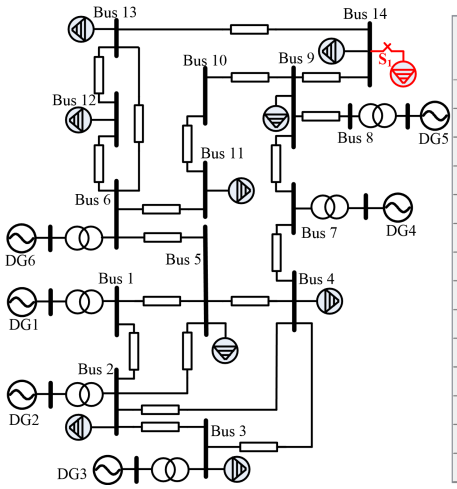

Bus No.	Load Power	
	P (MW)	Q (MVar)
1	–	–
2	53.5	11.4
3	69.5	15
4	46.3	–
5	16.2	–
6	–	–
7	–	–
8	–	–
9	100.3	12.4
10	–	–
11	57.7	1.3
12	133.5	10.8
13	190	-17.6
14	173	-10.5

Figure 12. 14-bus 6-DG test system (with the load power at each bus).

1) Scenario A- a step load disturbance: In Scenario A, a load step event occurs at $t = 1s$. Fig. 13 shows the simulation results (herein ΔP_1 of DG1 is selected for the demonstration). The fixed-gain PID and HDP-PID power control are both considered. We observe that (i) using fixed-gain PID control, the system frequency is prone to be less damped (resulting in a large drop slope, a small nadir and a salient overshoot); (ii) Using HDP-PID power control, the test system has a relatively smooth and well-damped frequency profile.

2) Scenario B- an uncertain load disturbance: In Scenario B, an uncertain load disturbance is considered. The uncertain load ΔP_{load}, with a power profile displayed in Fig. 14, is picked up at $t = 1s$. Fig. 14 also illustrates the simulation results. On one hand, much more severe frequency transients are observed when DGs fitted with the fixed-gain PID control. This is because that the fixed-gain PID control has less adaptivity to the uncertain disturbances and consequently the system would be more vulnerable to the load uncertainties. On the other hand, the HDP-PID power control enables well-improved frequency transients for both test systems. It helps that the HDP is a learning technology and enables the power control much more adaptive to the load uncertainties. Thus, the results claim that the HDP-PID power control outperforms the fixed-gain PID power control in stabilizing the islanded microgrids against uncertainties.

In addition, the HDP-PID control could enable DGs to have a more accurate power sharing, compared to the fixed-gain PID control. This is demonstrated from Fig. 15, where an uncertain disturbance appears in the 14-Bus test system. Actually, the

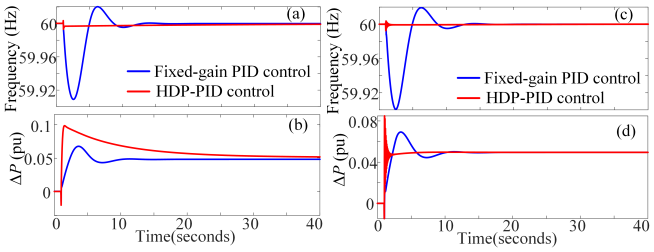

Figure 13. Responses of DGs versus a step load disturbance: (a)-(b) for 2-DG system and (c)-(d) for 14-Bus test system.

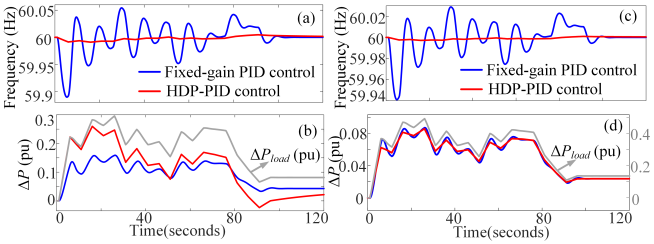

Figure 14. Responses of DGs versus an uncertain load disturbance: (a)-(b) for 2-DG system and (c)-(d) for 14-Bus test system.

frequency is a global variable which results in an accurate active power sharing among DGs for both controls (the active power responses of DGs are not displayed here).

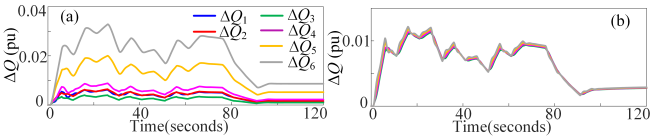

Figure 15. Reactive power responses of DGs in the 14-Bus test system versus an uncertain load disturbance: (a) installing a fixed -gain PID control; (b) installing an HDP-PID control.

3) Comparative simulations to the communication-based control: In this segment, we try to compare the control performance of the proposed HDP-PID control to the communication-based power control. The consensus-droop control in [34] is employed hereafter. The key parameters (with the notations reference to [34]) are set as $J = 20$, $D_p = 15$, $k_p = 1$, $k_q = 1$, $D_q = 10$ (where J is the inertia parameter). The communication network is naturally modeled as an undirected and connected graph.

The 14-Bus test system is used and an uncertain load disturbance is considered (like Scenario B). Fig. 16 displays the responses of DGs with the consensus-droop control and the HDP-PID control. It shows that the HDP-PID power control is advantageous over the consensus-droop control when coping with the uncertain disturbances.

4) Scenario C- specific sudden disturbances: In this segment, the HDP-PID control performance versus specific sudden changes is simulated. At first, we consider the grid topology change of the 14-Bus test system. The topology is modified with the removal of six transmission lines (that link Bus 1-2, Bus 2-4, Bus 2-3, Bus 7-9, Bus 9-14, Bus 12-13) at $t = 21s$. In addition, a step load increment is considered at

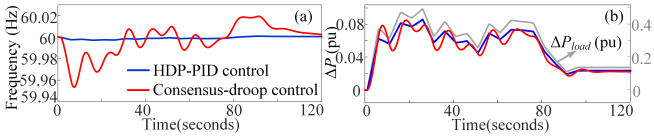

Figure 16. Responses of DGs versus an uncertain load disturbance (with the HDP-PID control or consensus-droop control used).

$t = 51s$. Fig. 17 depicts the DGs' responses. The result is that the proposed HDP-PID control is able to cope with the grid topology change.

Then, a sudden change to the switch-in/out of a DG is considered. However, the proposed HDP-PID power control would fail in restoring the power sharing of the rest DGs. The reason may be that relatively large changes of the frequency and its derivative are created during the sudden large power flow change. This would require undue learning and lead to the failure of the HDP-PID control. The improvement strategies will be investigated in a future paper.

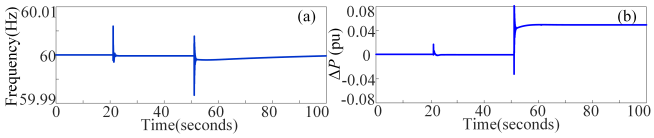

Figure 17. Responses of DGs versus a grid topology change of the 14-Bus test system.

VI. Conclusion

We have shown that the dynamic stability of PID power control is very sensitive to the operating conditions. This problem is relevant in islanded microgrids, where the interconnected lines have a low X/R ratio and the output power level of DGs is closely dependent on the pick-up loads. Using the proposed SFR model of DGs, a dynamic stability analysis is conducted for an islanded microgrid system. The results show that the critical eigenvalues of islanded systems directly vary with the operating condition and would lose stability under a heavy load and a loosely-interconnected network condition. This claims that the fixed-gain PID power control may not be able to effectively preserve the frequency quality and power sharing during load uncertainties. By using the learning algorithm, the HDP-PID power control is capable of ensuring the control performance against uncertain disturbances. With such control, it is conceivable to achieve an improvement of both the power sharing and the system stability during frequent load changes and uncertainties in islanded microgrids. These have been tested and validated by the simulations.

VII. Appendix

A. Proof of Theorem 1

The following provides the proof of Theorem 1. Here, the Lyapunov function candidate is selected as below

$$L = L_c + L_a \tag{40}$$

where $L_c = tr\left\{\widetilde{W}_c^T\widetilde{W}_c\right\}/2l_c$ and $L_a = tr\left\{\widetilde{W}_a^T\widetilde{W}_a\right\}l_c/2l_a$. Under Assumption 1, we have

$$\begin{aligned}\dot{L}_c &= (1/l_c)tr\left\{\widetilde{W}_c^T\dot{\widetilde{W}}_c\right\}\\ &= (1/l_c)tr\left\{\widetilde{W}_c^T\left[-l_c\sigma_c(\sigma_c^T\widetilde{W}_c+\varepsilon_h)\right]\right\}\\ &\le -\left(\sigma_{cm}^2-\frac{l_c}{2}\sigma_{cM}^2\right)\left\|\widetilde{W}_c\right\|^2+\frac{1}{2l_c}\varepsilon_h^2\end{aligned} \tag{41}$$

$$\begin{aligned}\dot{L}_a &= (l_c/l_a)tr\left\{\widetilde{W}_a^T\dot{\widetilde{W}}_a\right\}\\ &= (l_c/l_a)tr\left\{\widetilde{W}_a^T\left[-l_a\phi_a(\widetilde{W}_a^T\phi_a\right.\right.\\ &\quad\left.\left.+(1/2)R^{-1}B_u\nabla\phi_c^T\widetilde{W}_c+\varepsilon_{ca})^T\right]\right\}\\ &\le -\left[l_c\phi_{am}^2-(3/4)l_cl_a\phi_{aM}^2\right]\left\|\widetilde{W}_a\right\|^2\\ &\quad+\frac{l_c}{4l_a}\left\|R^{-1}\right\|^2\|B_u\|^2\phi_{dM}^2\left\|\widetilde{W}_c\right\|^2+\frac{l_c}{2l_a}\varepsilon_{ca}^T\varepsilon_{ca}\end{aligned} \tag{42}$$

Thus, the time derivative of (40) is given by

$$\begin{aligned}\dot{L} =& -\left(\sigma_{cm}^2-\frac{l_c}{2}\sigma_{cM}^2-\frac{l_c}{4l_a}\left\|R^{-1}\right\|^2\|B_u\|^2\phi_{dM}^2\right)\left\|\widetilde{W}_c\right\|^2\\ &-l_c\left[\phi_{am}^2-(3/4)l_a\phi_{aM}^2\right]\left\|\widetilde{W}_a\right\|^2\\ &+\frac{1}{2l_c}\varepsilon_h^2+\frac{l_c}{2l_a}\varepsilon_{ca}^T\varepsilon_{ca}\end{aligned} \tag{43}$$

Selecting l_c and l_a to satisfy

$$\begin{aligned}l_c &< \left(4l_a\sigma_{cm}^2\right)/\left(2l_a\sigma_{cM}^2+\left\|R^{-1}\right\|^2\|B_u\|^2\phi_{dM}^2\right)\\ l_a &< \left(4\phi_{am}^2\right)/\left(3\phi_{aM}^2\right)\end{aligned} \tag{44}$$

it enables $\dot{L}<0$ under admissible $\left\|\widetilde{W}_c\right\|$ and $\left\|\widetilde{W}_a\right\|$. Therefore, using Lyapunov theory, it claims that the network weight estimation errors $\widetilde{W}_c$ and $\widetilde{W}_a$ are UUB.

Hereafter, we attend to prove that $\|\hat{u}-u\|\le\varepsilon_u$ as $t\to\infty$. Revisiting (31), we have (45) for a small positive constant ε_v.

$$\widetilde{v}-v=\widetilde{W}_a^T\phi_a\le\varepsilon_v \tag{45}$$

when $t\to\infty$. Moreover in (31), u is a function of v. Thus,

$$\widetilde{u}-u\le(1/2)(1-u^2)\varepsilon_v\le\varepsilon_u \tag{46}$$

when ε_u is a positive constant.

B. DG Parameters (on Base of Machine Rating) [28]

$P_n = 2MW, V_n = 575V, \omega_0 = 120\pi$, filter resistance: $R_f = 0.003$pu, $L_f = 0.2$pu, $C_f = 0.057$pu, DC capacitor: $C_{dc} = 90000\mu F$, DC voltage: $V_{dc} = 1100V$, terminal-voltage control: $k_{pv} = 1, k_{iv} = 20$, DC voltage control: $k_{pdc} = 1.1, k_{idc} = 27.5$, current control: $k_{pi} = 1, k_{ii} = 50$, PLL control: $k_{pp} = 60, k_{ip} = 140$, Q-$\dot{V}$ control: $D_q = 10, k_q = 1$.

REFERENCES

[1] IEEE 2030.7, "IEEE Standard for the Specification of Microgrid Controllers," April 2018, [Online]. Available: https://ieeexplore.ieee.org/servlet/opac?punumber=8340142

[2] N. Pogaku, M. Prodanovic, and T. C. Green, "Modeling, analysis and testing of autonomous operation of an inverter-based microgrid," *IEEE Trans. Power Electron.*, vol. 22, no. 2, pp. 613-625, Mar. 2007.

[3] G. Rigatos, *Intelligent renewable energy systems: modelling and control*, Springer, 2016.

[4] P. L. Denholm, Y. Sun, and T. T. Mai, "An introduction to grid services: Concepts, technical requirements, and provision from wind," National Renewable Energy Lab.(NREL), Golden, CO (United States), Tech. Rep., 2019.

[5] M. C. Chandorkar, D. M. Divan, and R. Adapa, "Control of parallel connected inverters in standalone AC supply systems," *IEEE Trans. on Ind. Appl.*, vol. 29, no. 1, pp. 136-143, 1993.

[6] J. M. Guerrero, J. C. Vsquez, J. Matas, M. Castilla, and L. G. de Vicuna, "Control strategy for flexible microgrid based on parallel line-interactive UPS systems," *IEEE Trans. Ind. Electron.*, vol. 56, no. 3, pp. 726-736, Mar. 2009.

[7] M. F. Arani, and Y. A. R. I. Mohamed, "Analysis and impacts of implementing droop control in DFIG-based wind turbines on microgrid/weak-grid stability," *IEEE Trans. Power Syst.*, vol. 30, no. 1, pp. 385-396, Jan. 2015.

[8] H. Han, X. Hou, J. Yang, J. Wu, M. Su, and J. M. Guerrero, "Review of power sharing control strategies for islanding operation of AC microgrids," *IEEE Trans. Smart Grid*, vol. 7, no. 1, pp. 200-215, Jan. 2016.

[9] W. Du, Z. Chen, K. P. Schneider, R. H. Lasseter, S. P. Nandanoori, F. K. Tuffner, and S. Kundu, "A comparative study of two widely used grid-forming droop controls on microgrid small-signal stability," *IEEE J. Emerg. Sel. Topics Power Electron.*, vol. 8, no. 2, pp. 963-975, June 2020.

[10] E. Barklund, N. Pogaku, M. Prodanovic, C. Hernandez-Aramburo, T. C. Green. "Energy management in autonomous microgrid using stability-constrained droop control of inverters," *IEEE Trans. Power Electron.*, vol. 23, no. 5, pp. 2346-2352, 2008.

[11] Y. A. I. Mohamed, E. F. El-Saadany, "Adaptive decentralized droop controller to preserve power sharing stability of paralleled inverters in distributed generation microgrids," *IEEE Trans. Power Electron.*, vol. 23, no. 6, pp. 2806-2816, 2008.

[12] J. M. Guerrero, M. Chandorkar, T. Lee, and P. C. Loh, "Advanced control architectures for intelligent microgrids Part I: Decentralized and hierarchical control," *IEEE Trans. Ind. Electron.*, vol. 60, no. 4, pp. 1254-1262, Apr. 2013.

[13] M. Kabalan, P. Singh, and D. Niebur, "A design and optimization tool for inverter-based microgrids using large-signal nonlinear analysis," *IEEE Trans. Smart Grid*, vol. 10, no. 4, pp. 4566-4576, July 2019.

[14] L. Sun, K. Sun, Y. Hou, and J. Hu, "Optimized autonomous operation control to maintain the frequency, voltage and accurate power sharing for DGs in islanded systems," *IEEE Trans. Smart Grid*, vol. 11, no. 5, pp. 3885-3895, Sept. 2020.

[15] A. A. A. Radwan and Y. A. I. Mohamed, "Assessment and mitigation of interaction dynamics in hybrid AC/DC distribution generation systems," *IEEE Trans. Smart Grid*, vol. 3, no. 3, pp. 1382-1393, Sept. 2012.

[16] H. Moussa, A. Shahin, J. Martin, S. Pierfederici and N. Moubayed, "Optimal angle droop for power sharing enhancement with stability improvement in islanded microgrids," *IEEE Trans. Smart Grid*, vol. 9, no. 5, pp. 5014-5026, Sept. 2018.

[17] A. Kunwar, F. Shahnia and R. C. Bansald, "Eigenvalue-oriented dynamic stability examination to enhance designing a microgrid hosting clusters of inertial and non-inertial distributed generators," *IEEE Trans. Smart Grid*, vol. 11, no. 3, pp. 1942-1955, May 2020.

[18] Y. Han, M. Yang, P. Yang, et al., "Reduced-order model for dynamic stability analysis of single-phase islanded microgrid with BPF-based droop control scheme," *IEEE Access*, vol. 7, pp. 157859-157872, 2019.

[19] H. R. Baghaee, M. Mirsalim, and G. B. Gharehpetian, "Power calculation using RBF neural networks to improve power sharing of hierarchical control scheme in multi-DER microgrids," *IEEE J. Emerg. Sel. Topics Power Electron.*, vol. 4, no. 4, pp. 1217-1225, Dec. 2016.

[20] P. Kundur, *Power system stability and control*, New York: McGraw-Hill, 1994.

[21] P. M. Anderson, and M. Mirheydar, "A low-order system frequency response model," *IEEE Trans. Power Syst.*, vol. 5, no. 3, pp. 720-729, Aug. 1990.

[22] H. Zhang, L. Cui, X. Zhang and Y. Luo, "Data-driven robust approximate optimal tracking control for unknown general nonlinear systems using adaptive dynamic programming method," *IEEE Trans. Neural Netw.*, vol. 22, no. 12, pp. 2226-2236, Dec. 2011.
[23] M. Davari, W. Gao, Z. P. Jiang and F. L. Lewis, "An optimal primary frequency control based on adaptive dynamic programming for islanded modernized microgrids," *IEEE Trans. Autom. Sci. and Eng.*, vol. 18, no. 3, pp. 1109-1121, July 2021.
[24] Y. Tang, C. Mu, and H. He, "SMES based damping controller design using fuzzy-GrHDP considering transmission delay," *IEEE Trans. Appl. Supercond.*, vol. 26, no. 7, pp. 1C5, Oct. 2016.
[25] Y. Zhang, and B. T. Ooi, "Stand-alone doubly-fed induction generators (DFIGs) with autonomous frequency control," *IEEE Trans. Power Del.*, vol. 28, no. 2, pp. 752-760, Apr. 2013.
[26] D. Dong, J. Li, D. Boroyevich, P. Mattavelli, I. Cvetkovic, and Y. Xue, "Frequency behavior and its stability of grid-interface converter in distributed generation systems," in *Proc. 2012 IEEE Appl. Power Electron. Conf. Expo.*, 2012, pp. 1887-1893.
[27] A. M. Kulkarni, *Power system dynamics and control*, John Willey& Sons, Ltd, 2014.
[28] The MathWorks, September 2018 (Update January 2019). [Online]. Available: https://mathworks.com
[29] W. H. Kersting, *Distribution System Modeling and Analysis*, 3rd edition Boca Raton, FL, USA: CRC Press, 2012.
[30] F. L. wis, S. Jagannathan, and A. Yesildirek, *Neural network control of robot manipulators and nonlinear systems*, Taylor & Francis, 1999.
[31] B. Igelnik, and Y. H. Pao, "Stochastic choice of basis functions in adaptive function approximation and the functional-link net," *IEEE Trans. Neural Network*, vol. 6, no. 6, pp. 1320C1329, Nov. 1995.
[32] J. Sun, F. Liu, J. Si, and S. Mei, "Direct heuristic dynamic programming with augmented states," In *2011 International Joint Conference on Neural Networks. IEEE*, 2011.
[33] H. Zhang, L. Cui, X. Zhang and Y. Luo, "Data-driven robust approximate optimal tracking control for unknown general nonlinear systems using adaptive dynamic programming method," *IEEE Trans. Neural Network*, vol. 22, no. 12, pp. 2226-2236, Dec. 2011.
[34] L.-Y. Lu and C.-C. Chu, "Consensus-based droop control synthesis for multiple DICs in isolated micro-grids," *IEEE Trans. Power Syst.*, vol. 30, no. 5, pp. 2243C2256, Sep. 2014.

Li Sun received the B. Eng. degree and the M.Eng. degrees from Huazhong University of Science and Technology (HUST), Wuhan, China, in 2013, and 2016 respectively, and the Ph.D. degree from The University of Hong Kong, Hong Kong, in 2019, both in electrical engineering. After that she worked as a Research Fellow with the University of Warwick, United Kingdom until June 2021. She is currently an Assistant Professor with the School of Mechanical Engineering and Automation, Harbin Institute of Technology, Shenzhen, China. Her current research interests focus on the power system stability control, control design and optimization of islanded microgrids.

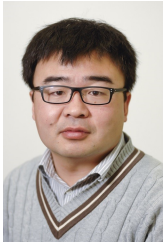

Xiaowei Zhao is Professor of Control Engineering and an EPSRC Fellow at the School of Engineering, University of Warwick, Coventry, UK. He obtained the PhD degree in Control Theory from Imperial College London in 2010. After that he worked as a postdoctoral researcher at the University of Oxford for three years before joining Warwick in 2013. His main research areas are control theory with applications on offshore renewable energy systems, local smart energy systems, and autonomous systems.

Yongfeng Lv received the B.S. and M.S. degrees in Mechatronic Engineering from Faculty of Mechanical and Electrical Engineering, Kunming University of Science and Technology, Kunming, China, in 2012 and 2016, and the Ph.D. degree in Control Science and Engineering with School of Automation, Beijing Institute of Technology, Beijing, China, in 2020. From 2012 to 2013, he served as an electromechanical technician in Shanxi Coal Transportation and Marketing Group, Linfen, Shanxi. Currently, he is a Lecturer with the College of Electrical and Power Engineering, Taiyuan University of Technology, Taiyuan, China, and also a research fellow with School of Engineering, University of Warwick, Coventry, UK. His current research interests include intelligent control, adaptive dynamic programming, smart energy systems and servo systems.